

Transition from geostrophic turbulence to inertia–gravity waves in the atmospheric energy spectrum

Jörn Callies ^{*}, Raffaele Ferrari [†], and Oliver Bühler [‡]

^{*}MIT/WHOI Joint Program in Oceanography, Cambridge/Woods Hole, MA, USA, [†]Earth, Atmospheric, and Planetary Sciences, Massachusetts Institute of Technology, Cambridge, MA, USA, and [‡]Courant Institute of Mathematical Sciences, New York University, New York, NY, USA

Submitted to Proceedings of the National Academy of Sciences of the United States of America

Midlatitude fluctuations of the atmospheric winds on scales of thousands of kilometers, the most energetic such fluctuations, are strongly constrained by the Earth’s rotation and the atmosphere’s stratification. As a result of these constraints, the flow is quasi-two-dimensional and energy is trapped at large scales—nonlinear turbulent interactions transfer energy to larger scales, but not to smaller scales. Aircraft observations of wind and temperature near the tropopause indicate that fluctuations at horizontal scales smaller than about 500 km are more energetic than expected from these quasi-two-dimensional dynamics. We present an analysis of the observations that indicates that these smaller-scale motions are due to approximately linear inertia–gravity waves, contrary to recent claims that these scales are strongly turbulent. Specifically, the aircraft velocity and temperature measurements are separated into two components: one due to the quasi-two-dimensional dynamics and one due to linear inertia–gravity waves. Quasi-two-dimensional dynamics dominate at scales larger than 500 km; inertia–gravity waves dominate at scales smaller than 500 km.

atmospheric dynamics | geostrophic turbulence | inertia–gravity waves

The mid-latitude high and low pressure systems visible in weather maps are associated with winds and temperature fluctuations that we experience as weather. These fluctuations arise from a baroclinic instability of the mean zonal winds at horizontal scales of a few thousand kilometers, commonly referred to as the synoptic scales [1, 2, 3]. The combined effects of rotation and stratification constrain the synoptic-scale winds to be nearly horizontal and to satisfy geostrophic balance, a balance between the force exerted by the changes in pressure and the Coriolis force resulting from Earth’s rotation. It is an open question whether the same constraints dominate in the mesoscale range, i.e. at scales of 10–500 km, or whether qualitatively different dynamics govern flows at these scales.

The synoptic-scale flows are turbulent in the sense that nonlinear scale interactions, which lie at the core of the difficulty to predict the weather, exchange energy between different scales of motion [4, 5, 6, 7]. Under the constraints of rotation and stratification, the synoptic-scale winds are approximately two-dimensional and non-divergent [8, 9]. In two-dimensional flows, nonlinear scale interactions tend to transfer energy to larger scales, i.e. the synoptic-scale pressure anomalies often merge and form larger ones, contrary to nonlinear scale interactions in three-dimensional flows, which tend to transfer energy to smaller scales [10]. Little energy is thus transferred to scales smaller than those at which the synoptic-scale fluctuations are generated through instabilities. Theory and numerical simulations predict that the energy per unit horizontal wavenumber k decays as rapidly as k^{-3} at wavenumbers larger than the wavenumber corresponding to the instability scale [9, 11]. This predicted kinetic energy spectrum is roughly consistent with synoptic-scale observations [9, 12].

Long-range passenger aircraft have been instrumented to collect velocity and temperature measurements as part of the Global Atmospheric Sampling Program in the 1970s and the Measurement of Ozone and Water Vapor by Airbus In-Service Aircraft (MOZAIC) project in the 1990s and 2000s. The resulting dataset, described in

the Materials and Methods section, consists of tens of thousand of flights. Because aircraft travel at altitudes between 9 and 14 km, the data largely reflect the upper troposphere and lower stratosphere, near the tropopause. These measurements confirm that the kinetic energy spectrum drops as k^{-3} in the synoptic wavenumber range, but there is a transition in behavior at a scale of about 500 km [13] (cf. Fig. 1*a*). In the mesoscale range, at scales smaller than 500 km, the kinetic energy spectrum decays more slowly, roughly like $k^{-5/3}$ [13, 14, 15].

The measured kinetic energy spectrum is intriguing, because it agrees so well with Charney’s theory of geostrophic turbulence at the synoptic scales [9], but deviates from that prediction at the mesoscale. The transition to the flatter $k^{-5/3}$ mesoscale spectrum has been interpreted as the signature of small-scale geostrophic flows generated by convective events [14, 16, 17], as the development of fronts at the edge of synoptic-scale cyclones and anticyclones at the top of the troposphere (equivalent to the warm and cold mesoscale fronts we experience at the Earth’s surface) [18], or as the signature of stratified turbulence at scales where the rotational constraints become less important [19]. These explanations of the synoptic-to-mesoscale transition invoke turbulent dynamics and strong interactions between the synoptic and mesoscale flows.

A rotating and stratified atmosphere, however, supports an additional, much faster set of motions: inertia–gravity waves. These are internal gravity waves, modified by the effect of rotation, that have periods of several minutes to a few hours. In contrast to the strongly nonlinear, turbulent synoptic-scale flow, these motions are wave-like and at small amplitude they are approximately governed by linear dynamics [20]. It has been proposed that the mesoscale energy is dom-

Significance

High and low pressure systems, commonly referred to as synoptic systems, are the most energetic fluctuations of wind and temperature in the midlatitude troposphere. Synoptic systems are a few thousand kilometers in scale and are governed by a balance between the pressure gradient force and the Coriolis force. Observations collected near the tropopause by commercial aircraft indicate a change in dynamics at horizontal scales smaller than about 500 km. Smaller-scale fluctuations are shown to be dominated by inertia–gravity waves, waves that propagate on vertical density gradients but are influenced by Earth’s rotation.

Reserved for Publication Footnotes

inated by inertia–gravity waves [21, 22], which are easily excited by any fast fluctuation of the atmospheric flows [23]. In this explanation of the mesoscale part of the spectrum, linear inertia–gravity and nonlinear synoptic-scale turbulence coexist with little interaction.

In this paper, we present an analysis of the MOZAIC data that utilizes a decomposition method recently developed by Bühler et al. [24]. For the first time, this new analysis provides compelling evidence that linear inertia–gravity waves indeed dominate the observations in the mesoscale.

Theories for the synoptic-to-mesoscale transition

Dewan first suggested that the mesoscale energy is dominated by a continuum of weakly nonlinear inertia–gravity waves [21]. VanZandt showed that the mesoscale spectra of horizontal wind fluctuations as a function of horizontal wavenumber, vertical wavenumber, and frequency are related through the dispersion and polarization relations of inertia–gravity waves [22]. The dominance of inertia–gravity waves at the mesoscale, however, appeared inconsistent with vertical velocity frequency spectra measured from radar in light-wind conditions [25]. More recently Vincent and Eckerman showed that the signature of inertia–gravity waves is recovered after correcting for Doppler-shift effects in radar observations [26].

In the last two decades, the interpretation of the synoptic-to-mesoscale transition in terms of inertia–gravity wave dynamics has received little attention. The $k^{-5/3}$ power-law dependence of the mesoscale spectrum has instead been interpreted as evidence that the mesoscale is strongly turbulent. The strong nonlinear interactions characteristic of turbulent flows continuously redistribute energy across wavenumbers and are known to result in power-law energy distributions [4, 7]. A number of competing turbulent theories have been proposed.

The earliest turbulent theory argues that the mesoscale spectrum is due to an inverse cascade of energy injected at even smaller scales, for example by convective activity [14, 16, 17]. The hypothesis is that nonlinear mesoscale interactions, much like at synoptic scales, transfer energy to larger scales because of the constraints of rotation and stratification. The kinetic energy spectrum in such a quasi-two-dimensional inverse cascade scales like $k^{-5/3}$ at wavenumbers smaller than the injection scale [11], in contrast to Charney’s k^{-3} spectrum, which develops at wavenumbers larger than the injection scale. The theory does not predict at which scale the dynamics switch from the synoptic to the mesoscale regime.

The second turbulent theory proposes that the flat mesoscale spectrum is the signature of sharp temperature fronts, which develop when synoptic-scale flows intersect a rigid boundary, like the Earth’s surface, or a strongly stratified layer, like the tropopause [18]. Importantly, the winds associated with the temperature fronts are still largely in geostrophic balance. In this view, the $k^{-5/3}$ mesoscale spectrum is a feature of measurements taken at the tropopause level, the cruising altitude of long range commercial aircraft, but should not appear in the mid troposphere. This prediction cannot be tested with available data.

The third turbulent theory proposes that the $k^{-5/3}$ mesoscale spectrum emerges at the scales where the flows escape the rotational constraint and energy can be transferred to smaller scales [19]. Turbulent flows constrained by stratification, but not rotation, are collectively known as “stratified turbulence”. The forward energy cascade is achieved by the overturning of layer-like structures. These flows are not in geostrophic balance, and thus differ from the quasi-two-dimensional dynamics of the previous two theories; and they are strongly nonlinear, and thus differ from approximately linear inertia–gravity waves.

Inertia–gravity waves and geostrophic flow

The understanding that atmospheric winds are composed of slow flows in approximate geostrophic balance and fast inertia–gravity waves has been the foundation for much progress in atmospheric sci-

ence. The first numerical weather predictions were based on quasi-geostrophic dynamics, an approximation to the more complete primitive equations that filters out inertia–gravity waves [27, 28, 29]. In the troposphere and lower stratosphere, inertia–gravity waves typically have small amplitudes and therefore interact only weakly with geostrophic flows. While there is a growing appreciation of rare instances of inertia–gravity waves directly influencing sensitive weather patterns [30], strong interactions between inertia–gravity waves and the geostrophic flow are typically confined to the middle and upper atmosphere, where the wave amplitude becomes large enough to allow for breaking of inertia–gravity waves and the concomitant drag force on the geostrophic flow that is well known to be crucial for the global angular momentum budget of the atmosphere [23].

In the deep ocean, breaking inertia–gravity waves mix heat and carbon. This leading-order effect has led to intensive study of the oceanic inertia–gravity wave field. It is composed of a continuous spectrum of linear waves together with isolated peaks at the inertial and tidal frequencies [31]. Similar to the lower atmosphere, these linear waves interact only weakly with the geostrophic flow. Only at small vertical scales of a few tens of meters do the waves break.

Callies and collaborators have recently shown that the energy spectra of oceanic flows are dominated by geostrophic flows at large scales and by inertia–gravity waves at small scales [24, 32]. The transition between the two classes of motion occurs at scales of 10–100 km, depending on the relative strength of the geostrophic eddies and the waves. In what follows, we show that the synoptic-to-mesoscale transition in the atmospheric kinetic energy spectrum is likely an equivalent transition from geostrophic to inertia–gravity wave dynamics.

Decomposition

From the MOZAIC aircraft observations of wind near the mid-latitude troposphere, we compute power spectra of the longitudinal (along-track) velocity u and transverse (across-track) velocity v , $S^u(k) = \langle |\hat{u}(k)|^2 \rangle$ and $S^v(k) = \langle |\hat{v}(k)|^2 \rangle$, where the caret denotes a Fourier transform and the angle brackets an average over flights. From the temperature observations, we compute the potential energy spectrum $S^b(k) = \langle |\hat{b}(k)|^2 \rangle / N^2$, where $b = g(\theta - \theta_0) / \theta_0$ is buoyancy, $g = 9.81 \text{ m s}^{-2}$ is the gravitational acceleration, $\theta_0 = 340 \text{ K}$ is the reference potential temperature, and N is the average vertical gradient of θ . Potential temperature is the temperature of an air parcel corrected for dynamically irrelevant compression effects. We use a typical stratification of the lower stratosphere, $N = 0.02 \text{ s}^{-1}$, estimated from the ERA-Interim reanalysis [33]. Fig. 1a shows that these MOZAIC spectra display the transition from a steep synoptic range to a flat mesoscale range at about 500 km.

If simultaneous wind and temperature observations were available in space and time, one could directly test whether the dispersion and polarization relations of inertia–gravity waves are satisfied by mesoscale motions. One could further separate out inertia–gravity waves and geostrophic flows, because inertia–gravity waves are restricted to frequencies between the Coriolis frequency f (equal to twice the rotation rate of the Earth multiplied by the sine of the latitude) and the buoyancy frequency N (the frequency at which a vertically displaced parcel of air will oscillate within the stably stratified atmosphere), while geostrophic flows evolve on much longer time scales. But it is extremely difficult to collect simultaneous measurements of mesoscale fluctuations of winds and temperature in space and time.

Bühler et al. have recently shown that the decomposition can be achieved from space-only measurements, provided that concurrent observations of horizontal velocities and temperature are available [24]. Applying this new decomposition to the MOZAIC data (see Materials and Methods) produces two powerful arguments in support of the hypothesis that the mesoscale spectrum is dominated by inertia–gravity waves.

First, assuming that the flow is an uncorrelated superposition of a geostrophic flow and inertia–gravity waves, we diagnose the inertia–gravity wave component of the total energy, the sum of the kinetic

and potential energies, solely based on the observed horizontal velocities. We then show that the thus predicted inertia–gravity wave energy spectrum closely matches the observed total energy spectrum in the mesoscale range. This indicates that the mesoscale potential energy spectrum, predicted by this procedure, is consistent with linear wave theory.

Second, assuming that the geostrophic component of the flow obeys Charney’s isotropy relation for geostrophic turbulence [9], we decompose the three observed individual spectra of longitudinal kinetic energy, transverse kinetic energy, and potential energy into a geostrophic component and an inertia–gravity wave component. The diagnosed inertia–gravity wave spectra closely match the observed spectra in the mesoscale range. This is another powerful test of the mesoscale flow’s consistency with the dispersion and polarization relations of inertia–gravity waves.

Helmholtz decomposition Fig. 1a shows that in the synoptic range, the spectra approximately satisfy Charney’s prediction for geostrophic turbulence: $S^u(k) = S^b(k)$ and $S^v(k) = 3S^u(k)$ [9, 12]. At the transition to the mesoscale, all three spectra converge. As shown by Lindborg and in the following, this convergence is evidence that the flow is no more in geostrophic balance at leading order [34, 35].

Any horizontal flow field can be decomposed into its rotational and divergent components: $u = -\psi_y + \phi_x$, $v = \psi_x + \phi_y$, where ψ is the streamfunction, ϕ is the velocity potential, x is the along-track coordinate, and y is the across-track coordinate. If the flow is statistically isotropic horizontally and ψ and ϕ are uncorrelated (as is the case for a superposition of geostrophic flow and linear inertia–gravity waves), the spectra $S^u(k)$ and $S^v(k)$ can be written in terms of spectral functions associated with ψ and ϕ (see Material and Methods):

$$S^u(k) = D^\psi(k) - k \frac{d}{dk} D^\phi(k), \quad [1]$$

$$S^v(k) = -k \frac{d}{dk} D^\psi(k) + D^\phi(k). \quad [2]$$

The spectral functions $D^\psi(k)$ and $D^\phi(k)$ can easily be computed from the observed $S^u(k)$ and $S^v(k)$ by solving the system of ordinary differential equations [1] and [2] (see Materials and Methods). Using $D^\psi(k)$ and $D^\phi(k)$, the observed kinetic energy spectrum $K(k) = \frac{1}{2}[S^u(k) + S^v(k)]$ can be decomposed into its rotational and divergent components,

$$K^\psi(k) = \frac{1}{2} \left(1 - k \frac{d}{dk} \right) D^\psi(k), \quad [3]$$

$$K^\phi(k) = \frac{1}{2} \left(1 - k \frac{d}{dk} \right) D^\phi(k). \quad [4]$$

The Helmholtz decomposition of the MOZAIC kinetic energy spectrum in Fig. 1b shows that the rotational component dominates in the synoptic range, whereas the divergent component becomes of the same order at the transition to the mesoscale range. In the mesoscale range, the divergent component slightly dominates over the rotational component.

The dominance of the rotational component in the synoptic scales is consistent with Charney’s geostrophic turbulence, because quasi-geostrophic flow is to leading order horizontally nondivergent. The significant divergent component in the mesoscale, on the other hand, is inconsistent with the mesoscale theories that rely on a leading-order geostrophic balance, namely the inverse-cascade theory and the frontogenesis theory. Instead, it points to the dominance of ageostrophic dynamics.

Lindborg also found that the rotational and divergent components of the flow are of the same order in the mesoscale range [35]. In his analysis, based on curve fitting and selective Fourier transforming, the rotational component slightly dominated the divergent component in the mesoscale range. He argued that this was inconsistent with inertia–gravity waves, for which he expected the divergent component

to be much larger than the rotational component. If the inertia–gravity wave field is dominated by near-inertial waves, however, as suggested by balloon measurements in the lower stratosphere [36], the rotational component is expected to be of the same order as the divergent component. In the following section, we show that the mesoscale signal is indeed consistent with linear inertia–gravity wave dynamics, i.e. with the dispersion and polarization relations of hydrostatic inertia–gravity waves.

Decomposition of the total energy spectrum into geostrophic and inertia–gravity wave components Geostrophic flows are horizontally nondivergent and therefore only have a rotational component, while inertia–gravity waves have both a rotational and a divergent component. To perform the decomposition into these two classes of motion, we note that the component of the total energy spectrum $E(k) = \frac{1}{2}[S^u(k) + S^v(k) + S^b(k)]$ that is due to hydrostatic inertia–gravity waves can be diagnosed from $D^\phi(k)$ alone (see Materials and Methods):

$$E_w(k) = 2K^\phi(k) = \left(1 - k \frac{d}{dk} \right) D^\phi(k), \quad [5]$$

where the subscript “w” designates the inertia–gravity wave component. This somewhat surprising result follows directly from linear inertia–gravity wave dynamics, if horizontal isotropy and vertical homogeneity are assumed. Provided there is no additional type of motion, the residual of the observed total energy spectrum can be attributed to a geostrophic flow: $E_g(k) = E(k) - E_w(k)$, where the subscript “g” designates the geostrophic component.

The decomposition into geostrophic flow and inertia–gravity waves of the MOZAIC data is shown in Fig. 1c. The mesoscale range is dominated by inertia–gravity waves, which do not contribute much energy at the synoptic scales. The residual spectrum, i.e. the total spectrum minus the inertia–gravity wave component, dominates at the synoptic scales. This component can be confidently attributed to geostrophic flows, because we have shown that the spectrum in the synoptic range is purely rotational and hence horizontally nondivergent. At the transition scale, the geostrophic component of the total energy keeps falling off steeply—the transition appears to be due to inertia–gravity waves becoming dominant in the mesoscale range. This is the main result of this paper.

Notice that the geostrophic spectrum keeps falling off steeply past the transition at 500 km, but eventually flattens out at smaller scales. This flattening is likely an artifact, because at these scales the geostrophic component makes up a small fraction of the observed signal. It is quite possible that the flattening is due to noise or biases introduced by the interpolation procedure or by truncation errors in the reported wind and temperature data.

Decomposition of kinetic and potential energy spectra We have shown that the total energy spectrum can be decomposed into its geostrophic and inertia–gravity wave components. To confirm that the observed spectra are consistent with geostrophic dynamics at synoptic scales and with inertia–gravity wave dynamics at mesoscales, we now decompose into its two components each of the atmospheric spectra, the longitudinal and transverse kinetic energy spectra, $S^u(k)$ and $S^v(k)$, and the potential energy spectrum, $S^b(k)$. This can be done if one makes one further assumption. Following Charney and results from numerical simulations of geostrophic turbulence, the geostrophic streamfunction is assumed to be three-dimensionally isotropic, with the vertical coordinate rescaled by f/N [9]. This implies $S_g^u(k) = S_g^b(k)$, a relation that we noted is satisfied by the observed spectra in the synoptic range (Fig. 1a).

This decomposition—obtained by applying [15]–[17] and [20]–[22], given in the Materials and Methods section—confirms the main conclusion that the observed synoptic-scale flow is consistent with geostrophic dynamics and that the observed mesoscale flow is consistent with inertia–gravity wave dynamics. In the synoptic range,

the observed spectra match the diagnosed geostrophic components (Fig. 2a). At the transition scale, the diagnosed geostrophic spectra start deviating from the observed spectra and keep falling off steeply. At this scale, the diagnosed inertia–gravity wave spectra become comparable to the observed spectra and start matching them in the mesoscale range (Fig. 2b).

Discussion

Our analysis shows that the aircraft observations are consistent with a geostrophic flow that dominates the synoptic range and with inertia–gravity waves that dominate the mesoscale range. This conclusion is predicated on the assumption that the total observed flow is a superposition of geostrophic flow and inertia–gravity waves and that these two components are uncorrelated and horizontally isotropic.

In accord with Lindborg’s result [34], our analysis conclusively shows that mesoscale flows are not in geostrophic balance, thus falsifying previous suggestions that mesoscale spectra represent geostrophic eddies generated by atmospheric convective events or geostrophically balanced fronts at the tropopause. Our analysis then further shows that the observed mesoscale spectra $S^u(k)$, $S^v(k)$, and $S^b(k)$ are consistent with the dispersion and polarization relations of linear hydrostatic inertia–gravity waves. Presumably, it would be very surprising if the strongly nonlinear ageostrophic flows characteristic of stratified turbulence were to yield the same relations between these mesoscale spectra as the linear waves.

A similar transition between a dominant geostrophic flow at large scales and dominant inertia–gravity waves at small scales is well established in the oceanic spectra [32], providing further support for our interpretation of the synoptic-to-mesoscale transition. The ocean, like the atmosphere, is a strongly rotating and stratified fluid. The most energetic large-scale fluctuations are generated by baroclinic instabilities in both fluids, while small-scale inertia–gravity waves are triggered by any fast perturbation. A posteriori, it should not be surprising that both fluids exhibit a transition from geostrophic dynamics at large scales to inertia–gravity wave dynamics at small scales.

That inertia–gravity waves dominate the mesoscale spectrum does not mean that the atmosphere is filled with a nearly uniform and stationary wave field, as appears to be the case in the ocean [31]. The atmospheric wave field is likely highly intermittent in both space and time [23]. Our result merely suggests that on average, inertia–gravity waves dominate the mesoscale range. A good understanding of what sets the shape of the average atmospheric inertia–gravity wave spectrum is lacking. The oceanic inertia–gravity wave spectrum, however, has been shown to be an equilibrium solution of weakly interacting inertia–gravity waves with slopes close to $k^{-5/3}$ [37, 38]. While the residence time of waves in the atmosphere is shorter and shears provided by jet streams stronger, weak turbulence theory may similarly yield insight into the atmospheric inertia–gravity wave field.

The spatial patterns of mesoscale energy are also consistent with the dominance of inertia–gravity waves at the mesoscales. The aircraft spectra in the mesoscale range are up to six times larger in mountainous regions than over flat terrain [39]. The inertia–gravity wave activity is expected to be enhanced over mountains, where lee waves are excited by large- and synoptic-scale flows impinging on topography. Stratified turbulence, on the other hand, is fed directly by synoptic-scale energy and therefore not expected to be enhanced over mountainous regions.

High-resolution numerical models reproduce the synoptic-to-mesoscale transition [40]. Model results are consistent with the observation that the synoptic range is dominated by rotational flow, while the rotational and divergent components are of the same order in the mesoscale range [41, 42]. Models also show a pattern of enhanced mesoscale energies in regions of high topography [42]. The simulations further show that the mesoscale spectrum is not the result of

stratified turbulence [43], in agreement with our conclusion that they are the signature of inertia–gravity waves.

The emergent picture is relatively simple. Geostrophic synoptic-scale baroclinic disturbances force a forward enstrophy cascade that continues through the synoptic-to-mesoscale transition. The k^{-3} or slightly steeper geostrophic spectrum is masked by inertia–gravity waves at scales smaller than 500 km. This picture does not rule out the possibility that some fraction of the energy in the mesoscale spectra is associated with fronts and stratified turbulence, but these contributions must be small.

The result of this paper may also have some implications for the theoretical predictability of atmospheric flows. Lorenz argued that a turbulent flow with a $k^{-5/3}$ kinetic energy spectrum has a finite predictability time, which is of the order of the eddy turnover time [6]. More and more accurate knowledge of the initial state cannot push forecasts beyond that limit—even if we had a perfect model. In contrast, turbulent flows with a k^{-3} kinetic energy spectrum do not have such a predictability limit and ever more accurate initial conditions can lead to ever longer forecasts.

If the flat mesoscale spectrum were due to a turbulent cascade, that would pose a limit on predictability of synoptic systems [7, 44]. Observing and modeling the atmosphere beyond the transition at 500 km would yield rapidly diminishing returns in predictability. If this part of the spectrum is due to inertia–gravity waves, however, improving observational systems and forecast models may not prove as futile. Inertia–gravity waves do not propagate errors in the same way as the turbulent flows discussed by Lorenz. If the geostrophic component of the mesoscale flow were to be observed, despite the dominance of inertia–gravity waves, the forecast times of synoptic systems could potentially be extended considerably.

It should be noted, however, that other processes not considered in this theoretical argument may affect predictability. Moist convective processes, for example, lead to rapid growth of errors that can leak into the geostrophic flow [45]. Currently, the practical predictability of the weather is likely limited by inadequate representation of such processes.

Materials and Methods

Aircraft data. The spectra shown in Fig. 1a are calculated from wind and temperature measurements obtained by the MOZAIC program, which equipped commercial aircraft with instrumentation to measure trace gases, but also records wind speed and direction from the board computer. The data used here were obtained in 2002–2010 and are restricted to the northern hemisphere midlatitudes (30 to 60 degrees latitude). Great circles are fit to the flight paths and segments are discarded if they are shorter than 6,000 km, the average sample spacing is coarser than 1.2 km, or the deviation from the great circle is greater than 2 degrees. The data are then linearly interpolated onto a regular grid with 1 km spacing. Data at pressures larger than 350 hPa are discarded. Subsequently, for each flight, data deviating more than 1 km in altitude from the mean altitude are also discarded. Temperature data are adjusted to account for remaining variations in flight altitude, assuming a constant stratification $N = 0.02 \text{ s}^{-1}$, but this correction is of no consequence for the results discussed in the main paper. Nastrom and Gage [13] and Cho and Lindborg [15] showed that the spectral shapes are qualitatively the same in the upper troposphere and lower stratosphere, thus we do not separate the data into vertical bins. Spectra are computed by applying a Hann window, compensating for the variance loss, performing a discrete Fourier transform, and averaging over all 458 segments. The windowing is necessary to prevent spectral leakage of synoptic-scale energy into the mesoscale. Spectra at wavelengths smaller than 20 km are discarded because they are potentially affected by the interpolation procedure or by truncation errors in the reported data. Locations were reported in longitude/latitude with an accuracy of 0.01 degrees; zonal and meridional winds were reported with an accuracy of 0.01 m s^{-1} ; temperatures were reported with an accuracy of 0.01 K. These noise levels do not affect the spectra on scales larger than 20 km. We also discard the largest resolved wavelength, because the power at this wavelength is reduced artificially by the window.

Details of decomposition. We here give more detail on the decomposition techniques used to analyze the aircraft spectra. Bühler et al. give a more comprehensive description of these techniques and illustrate their skill to analyze oceanic spectra [24].

Let u and v be horizontal velocity components defined in the xy -plane with x aligned with the aircraft track, so u is the longitudinal (along-track) component and v is the transverse (across-track) component. The time t and altitude z are considered fixed during the measurement, so they will be ignored. Now, a general two-dimensional flow has a Helmholtz decomposition into rotational and divergent components of the form $u = -\psi_y + \phi_x$ and $v = \psi_x + \phi_y$. The functions ψ and ϕ are uniquely determined in terms of the velocity field with doubly periodic boundary conditions.

Progress with the statistical theory is possible if $\psi(x, y)$ and $\phi(x, y)$ are uncorrelated. We can then write the two-dimensional power spectra of u and v as

$$S^u(k, l) = l^2 S^\psi(k, l) + k^2 S^\phi(k, l), \quad [6]$$

$$S^v(k, l) = k^2 S^\psi(k, l) + l^2 S^\phi(k, l), \quad [7]$$

where l is the across-track wavenumber. Integration over l and some manipulation gives [1] and [2] with

$$D^\psi(k) = \frac{1}{\pi} \int_k^\infty \sqrt{k_h^2 - k^2} S^\psi(k_h) dk_h, \quad [8]$$

$$D^\phi(k) = \frac{1}{\pi} \int_k^\infty \sqrt{k_h^2 - k^2} S^\phi(k_h) dk_h, \quad [9]$$

where $S^\psi(k_h)$ and $S^\phi(k_h)$ are the two-dimensional isotropic spectra of ψ and ϕ , related to the two-dimensional spectra by $S(k_h) = 2\pi k_h S(k, l)$, $k_h = \sqrt{k^2 + l^2}$ is the magnitude of the horizontal wavenumber vector, and $k \geq 0$ is the along-track wavenumber.

The equations [1] and [2] can be solved explicitly, given the boundary conditions $D^\psi(\infty) = 0$ and $D^\phi(\infty) = 0$,

$$D^\psi(s) = \int_s^\infty [S^u(\sigma) \sinh(s - \sigma) + S^v(\sigma) \cosh(s - \sigma)] d\sigma, \quad [10]$$

$$D^\phi(s) = \int_s^\infty [S^u(\sigma) \cosh(s - \sigma) + S^v(\sigma) \sinh(s - \sigma)] d\sigma, \quad [11]$$

where for convenience the coordinate was transformed to $s = \ln k$.

Relation [5] follows from the dispersion and polarization relations of hydrostatic inertia-gravity waves. Combining the vorticity and continuity equations of the linearized primitive equations yields $\nabla^2 \psi_t = f \nabla^2 \phi$ [20], which implies that

$$S^\psi(k, l, \omega) = \frac{f^2}{\omega^2} S^\phi(k, l, \omega) \quad [12]$$

and thus, with the use of [6] and [7],

$$S^u(k, l, \omega) + S^v(k, l, \omega) = \left(1 + \frac{f^2}{\omega^2}\right) (k^2 + l^2) S^\phi(k, l, \omega). \quad [13]$$

The linear buoyancy equation is $b_t + N^2 w = 0$ and the potential energy spectrum $S^b(k) = \langle |\hat{b}(k)|^2 \rangle / N^2$ can also be related to the spectrum of the velocity potential,

$$S^b(k, l, \omega) = \left(1 - \frac{f^2}{\omega^2}\right) (k^2 + l^2) S^\phi(k, l, \omega), \quad [14]$$

if uncorrelated plane waves or equivalently vertical homogeneity is assumed. A slowly varying background is allowed. Adding [13] and [14] then eliminates the dependence on ω , so that [5] follows by integrating over l and ω .

The decomposition of the three individual spectra can be achieved by decomposing $D^\psi(k) = D_g^\psi(k) + D_w^\psi(k)$. The divergent part $D^\phi(k)$ needs no such decomposition, because the geostrophic component of the flow is divergence-free. Using

$$S_g^u(k) = D_g^\psi(k), \quad [15]$$

$$S_g^v(k) = -k \frac{d}{dk} D_g^\psi(k), \quad [16]$$

$$S_g^b(k) = D_g^\psi(k), \quad [17]$$

where Charney's assumption $S_g^b(k) = S_g^u(k)$ was applied, we can write the total energy spectrum of the geostrophic component $E_g(k) = \frac{1}{2}[S_g^u(k) + S_g^v(k) + S_g^b(k)]$ as

$$E_g(k) = \left(1 - \frac{k}{2} \frac{d}{dk}\right) D_g^\psi(k). \quad [18]$$

Since $E_g(k) = E(k) - E_w(k)$ can be diagnosed from the observations and [5], this can be solved for $D_g^\psi(k)$:

$$D_g^\psi(s) = 2 \int_s^\infty E_g(\sigma) e^{2(s-\sigma)} d\sigma, \quad [19]$$

where the boundary condition $D_g^\psi(\infty) = 0$ was used and the coordinate was again transformed to $s = \ln k$ for convenience. The decomposition is now complete. The wave spectra are

$$S_w^u(k) = D_w^\psi(k) - k \frac{d}{dk} D_w^\phi(k), \quad [20]$$

$$S_w^v(k) = -k \frac{d}{dk} D_w^\psi(k) + D_w^\phi(k), \quad [21]$$

$$S_w^b(k) = \left(1 - k \frac{d}{dk}\right) [D_w^\phi(k) - D_w^\psi(k)], \quad [22]$$

where $D_w^\psi(k) = D^\psi(k) - D_g^\psi(k)$, $D_w^\phi(k) = D^\phi(k)$, and [5] was used to deduce the last equation.

ACKNOWLEDGMENTS. We thank the principal investigators of the MOZAIC project, the European Commission for supporting the MOZAIC project, ETHER (CNES-CNRS/INSU) for hosting the database, and the participating airliners for transporting the instrumentation free of charge. OB gratefully acknowledges financial support under grants NSF-CMG-1024180, NSF-DMS-1312159, and NSF-DMS-1009213. JC and RF thank Glenn Flierl for offering useful feedback during the preparation of the manuscript and acknowledge financial support under grants ONR-N-00014-09-1-0458 and NSF-CMG-1024198.

1. Charney JG (1947) The dynamics of long waves in a baroclinic westerly current. *J Meteorol* 4:135–162.
2. Eady ET (1949) Long Waves and Cyclone Waves. *Tellus* 1:33–52.
3. Phillips NA (1954) Energy Transformations and Meridional Circulations associated with simple Baroclinic Waves in a two-level, Quasi-geostrophic Model. *Tellus* 6:273–286.
4. Batchelor GK (1953) *The Theory of Homogeneous Turbulence* (Cambridge University Press, London), pp 197.
5. Lorenz EN (1963) Deterministic Nonperiodic Flow. *J Atmos Sci* 20:130–141.
6. Lorenz EN (1969) The predictability of a flow which possesses many scales of motion. *Tellus* 21:289–307.
7. Vallis GK (2006) *Atmospheric and Oceanic Fluid Dynamics* (Cambridge University Press, Cambridge), pp 745.
8. Rossby CG (1939) Relation between variations in the intensity of the zonal circulation of the atmosphere and the displacements of the semi-permanent centers of action. *J Mar Res* 2:38–55.
9. Charney J (1971) Geostrophic Turbulence. *J Atmos Sci*, 28:1087–1095.
10. Fjørtoft R (1953) On the Changes in the Spectral Distribution of Kinetic Energy for Twodimensional, Nondivergent Flow. *Tellus* 5:225–230.
11. Kraichnan RH (1963) Inertial Ranges in Two-Dimensional Turbulence. *Phys Fluids* 10:1417–1423.
12. Leith CE (1971) Atmospheric Predictability and Two-Dimensional Turbulence. *J Atmos Sci* 28:145–161.
13. Nastrom GD, Gage KS (1985) A Climatology of Atmospheric Wavenumber Spectra of Wind and Temperature Observed by Commercial Aircraft. *J Atmos Sci* 42:950–960.
14. Gage KS (1979) Evidence for a $k^{-5/3}$ Law Inertial Range in Mesoscale Two-Dimensional Turbulence. *J Atmos Sci* 36:1950–1954.
15. Cho JYN, Lindborg E (2001) Horizontal velocity structure functions in the upper troposphere and lower stratosphere: 1. Observations. *J Geophys Res* 106:D10.
16. Lilly DK (1983) Stratified Turbulence and the Mesoscale Variability of the Atmosphere. *J Atmos Sci* 40:749–761.
17. Vallis GK, Shutts GJ, Gray MEB (1997) Balanced mesoscale motion and stratified turbulence forced by convection. *Q J R Meteorol Soc* 123:1621–1652.
18. Tulloch R, Smith KS (2006) A theory for the atmospheric energy spectrum: Depth-limited temperature anomalies at the tropopause. *Proc Natl Acad Sci USA*, 103:14690–14694.
19. Lindborg E (2006) The energy cascade in a strongly stratified fluid. *J Fluid Mech*, 550:207–242.
20. Pedlosky J (2010) *Waves in the Ocean and Atmosphere* (Springer, Berlin), pp 260.
21. Dewan EM (1979) Stratospheric Wave Spectra Resembling Turbulence. *Science*, 204:832–834.
22. VanZandt TE (1982) A universal spectrum of buoyancy waves in the atmosphere. *Geophys Res Lett*, 9:575–578.
23. Fritts DC, Alexander MJ (2003) Gravity wave dynamics and effects in the middle atmosphere. *Rev Geophys* 41:1003.

24. Bühler O, Callies J, Ferrari R (2014) Wave–vortex decomposition of one-dimensional ship track data. *J Fluid Mech* (in press).
25. Gage KS, Nastrom GD (1985) On the spectrum of atmospheric velocity fluctuations seen by MST/ST radar and their interpretation. *Radio Sci* 20:1339–1347.
26. Vincent RA, Eckermann SD (1990) VHF radar observations of mesoscale motions in the troposphere: Evidence for gravity wave Doppler shifting. *Radio Sci* 25:1019–1037.
27. Charney JG (1949) On the physical basis for numerical prediction of large-scale motions in the atmosphere. *J Meteorol* 6:371–385.
28. Charney JG, Eliassen A (1949) A Numerical Method for Predicting the Perturbations of the Middle Latitude Westerlies. *Tellus* 1:38–54.
29. Charney JG, Fjørtoft R, von Neumann J (1950) Numerical Integration of the Barotropic Vorticity Equation. *Tellus* 2:237–254.
30. Ruppert JH, Jr, Bosart LF (2014) A Case Study of the Interaction of a Mesoscale Gravity Wave with a Mesoscale Convective System. *Mon Wea Rev* 142:1403–1429.
31. Garrett C, Munk W (1979) Internal waves in the ocean. *Ann Rev Fluid Mech*, 11:339–369.
32. Callies J, Ferrari R (2013) Interpreting Energy and Tracer Spectra of Upper-Ocean Turbulence in the Submesoscale Range (1–200 km). *J Phys Oceanogr* 43:2456–2474.
33. Dee DP, et al. (2011) The ERA-Interim reanalysis: configuration and performance of the data assimilation system. *Q J R Meteorol Soc* 137:553–597.
34. Lindborg E (1999) Can the atmospheric kinetic energy spectrum be explained by two-dimensional turbulence? *J Fluid Mech* 388:259–288.
35. Lindborg E (2007) Horizontal Wavenumber Spectra of Vertical Vorticity and Horizontal Divergence in the Upper Troposphere and Lower Stratosphere. *J Atmos Sci* 64:1017–1025.
36. Hertzog A, Vial F, Mechoso C-R, Basdevant C, Cocquerez P (2002) Quasi-Lagrangian measurements in the lower stratosphere reveal an energy peak associated with near-inertial waves. *Geophys Res Lett*, 29:70-1–70-4.
37. McComas CH, Müller P (1981) The Dynamic Balance of Internal Waves. *J Phys Oceanogr* 11:970–986.
38. Polzin KL, Lvov YV (2011) Toward Regional Characterizations of the Oceanic Internal Wavefield. *Rev Geophys* 49:RG4003.
39. Nastrom GD, Fritts DC, Gage KS (1987) An Investigation of Terrain Effects on the Mesoscale Spectrum of Atmospheric Motions. *J Atmos Sci* 44:3087–3096.
40. Koshyk JN, Hamilton K, Mahlman JD (1999) Simulation of the $k^{-5/3}$ mesoscale spectral regime in the GFDL SKYHI general circulation model. *Geophys Res Lett* 26:843–846.
41. Koshyk JN, Hamilton K (2001) The Horizontal Kinetic Energy Spectrum and Spectral Budget Simulated by a High-Resolution Troposphere–Stratosphere–Mesosphere GCM. *J Atmos Sci* 58:329–348.
42. Hamilton K, Takahashi YO, Ohfuchi W (2008) Mesoscale spectrum of atmospheric motions investigated in a very fine resolution global general circulation model. *J Geophys Res* 113:D18110.
43. Skamarock WC, Park SH, Klemp JB, Snyder C (2014) Atmospheric Kinetic Energy Spectra from Global High-Resolution Nonhydrostatic Simulations. *J Atmos Sci* (under review).
44. Palmer TN (2000) Predicting uncertainty in forecasts of weather and climate. *Rep Prog Phys* 63:71–116.
45. Zhang F, Bei N, Rotunno R, Snyder C, Epifanio CC (2007) Mesoscale Predictability of Moist Baroclinic Waves: Convection-Permitting Experiments and Multistage Error Growth Dynamics. *J Atmos Sci* 64:3579–3594.

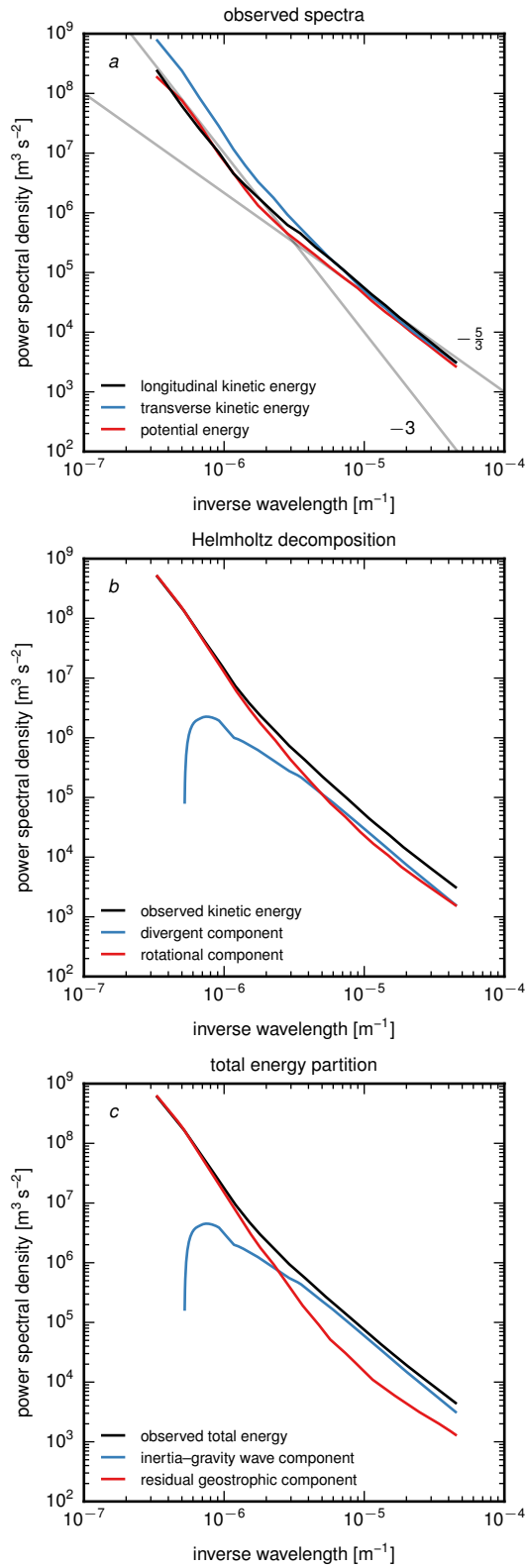


Fig. 1. Observed wavenumber spectra of near-tropopause midlatitude winds and decomposition into geostrophic component and inertia-gravity wave component. (a) Observed spectra of longitudinal kinetic energy $S^u(k)$, transverse kinetic energy $S^v(k)$, and potential energy $S^b(k)$. (b) Helmholtz decomposition of the observed kinetic energy spectrum $K(k)$ into its rotational and divergent components $K^\psi(k)$ and $K^\phi(k)$. (c) Partitioning of the total energy spectrum $E(k)$ into the diagnosed inertia-gravity wave component $E_w(k)$ and the residual geostrophic component $E_g(k)$.

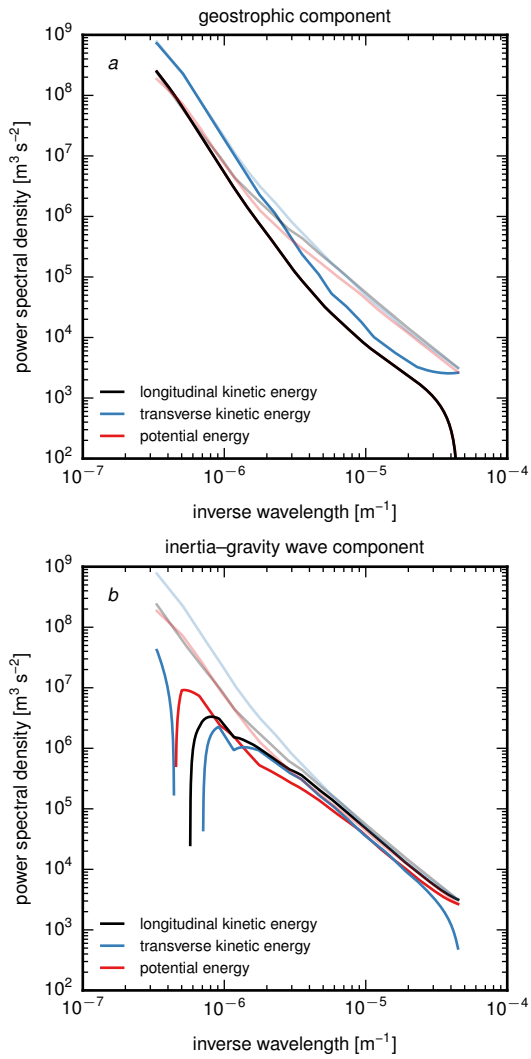


Fig. 2. Decomposition of observed wavenumber spectra into the geostrophic and inertia-gravity wave components. (a) Diagnosed geostrophic component of the spectra of longitudinal kinetic energy $S_g^u(k)$, transverse kinetic energy $S_g^v(k)$, and potential energy $S_g^b(k)$ (heavy lines) and observed spectra for reference (faint lines). Note that by construction $S_g^u(k) = S_g^b(k)$, so that the red and black heavy lines are on top of each other. (b) Diagnosed inertia-gravity wave component of the spectra of longitudinal kinetic energy $S_w^u(k)$, transverse kinetic energy $S_w^v(k)$, and potential energy $S_w^b(k)$ (heavy lines) and observed spectra for reference (faint lines). A blowup of the mesoscale range of this panel can be found in the Supporting Information.